Journal of Materials Science & Technology 209 (2025) 128–138

Contents lists available at ScienceDirect

Journal of Materials Science & Technology

journal homepage: www.elsevier.com/locate/jmst

Research Article

Simultaneous improvement of strength and ductility in a P-doped CrCoNi medium-entropy alloy

Hangzhou Zhang[a,b], Guoqiang Sun[c], Muxin Yang[a,b,*], Fuping Yuan[a,b], Xiaolei Wu[a,b]

[a] State Key Laboratory of Nonlinear Mechanics, Institute of Mechanics, Chinese Academy of Sciences, Beijing 100190, China
[b] School of Engineering Science, University of Chinese Academy of Sciences, Beijing 100049, China
[c] Department of Structural Steels, Central Iron and Steel Research Institute, Beijing 100081, China

ARTICLE INFO

Article history:
Received 29 February 2024
Revised 10 May 2024
Accepted 11 May 2024
Available online 28 May 2024

Keywords:
Tensile ductility
Dynamic grain refinement
Stacking fault energy
Strain hardening
Phosphorus segregation

ABSTRACT

A newly developed P-doped CrCoNi medium-entropy alloy (MEA) provides both higher yield strength and larger uniform elongation than the conventional CrCoNi MEA, even superior tensile ductility to the other-element-doped CrCoNi MEAs at similar yield strength levels. P segregation at grain boundaries (GBs) and dissolution inside grain interiors, together with the related lower stacking fault energy (SFE) are found in the P-doped CrCoNi MEA. Higher hetero-deformation-induced (HDI) hardening rate is observed in the P-doped CrCoNi MEA due to the grain-to-grain plastic deformation and the dynamic structural refinement by high-density stacking fault-walls (SFWs). The enhanced yield strength in the P-doped CoCrNi MEA can be attributed to the strong substitutional solid-solution strengthening by severer lattice distortion and the GB strengthening by phosphorus segregation at GBs. During the tensile deformation, the multiple SFW frames inundated with massive multi-orientational tiny planar stacking faults (SFs) between them, rather than deformation twins, are observed to induce dynamic structural refinement for forming parallelepiped domains in the P-doped CoCrNi MEA, due to the lower SFE and even lower atomically-local SFE. These nano-sized domains with domain boundary spacing at tens of nanometers can block dislocation movement for strengthening on one hand, and can accumulate defects in the interiors of domains for exceptionally high hardening rate on the other hand.

1. Introduction

Metals and alloys with high yield strength and large tensile ductility are always demanded in industrial applications [1,2]. The traditional strengthening methods, such as grain refinement strengthening [3,4], cold-working strengthening [5], precipitation strengthening [6], and solid-solution strengthening [7,8], can improve yield strength while inevitably resulting in the loss of tensile ductility. Grain boundary and dislocation strengthening generally can induce lower strain hardening, thus resulting in strain localization and reduced uniform elongation [3,9]. Stress concentration is usually induced at the phase boundaries in the precipitated alloys, and earlier cracks can be initiated at these boundaries for reduced tensile ductility [10]. It is well known that solid-solution strengthening is an efficient strategy to elevate yield strength without significantly sacrificing tensile ductility.

The addition of a small amount of interstitial elements with a small atom radius (such as C or N) in metals and alloys can improve their tensile properties significantly [11,12]. The interstitial elements can induce higher lattice friction to dislocation motion for strengthening on one hand, and can achieve higher dislocation storage and stronger strain hardening capacity on the other hand, through changing the glide pattern of dislocations by interacting with them [13]. The interstitial solution strengthening has been proven to be effective in enhancing both ductility and fracture toughness at high strength levels in metals and alloys [14,15]. However, the viewpoints on the effects of addition of a small amount of P element on the tensile properties were contradictory in the literature [16,17]. On one hand, it has been widely accepted that the segregation of P element at the grain boundaries leads to intergranular fracture along them [16,18]. Thus, one of standards for high-quality steels is the control of P element under 10 ppm [19]. On the other hand, it is well known that P element is the strongest element for substitutional solution strengthening ([P]~0.06-0.1 wt.%) in Fe-based or Ni-based alloys [20]. The addition of a small amount of P element can also promote the strain hardening ability in the dual-phase steels with

* Corresponding author.
E-mail address: mxyang@lnm.imech.ac.cn (M. Yang).

https://doi.org/10.1016/j.jmst.2024.05.020
1005-0302/

transformation-induced-plasticity (TRIP) effect [21]. Moreover, the addition of a small amount of P element can significantly increase the tensile ductility at high temperatures while with little influence on the room-temperature ductility for the Ni-based alloys [22]. In both ferritic and martensitic steels, as well as Ni-based high-temperature alloys, the addition of P element at levels of 10 times ppm has been shown to significantly influence their macroscopic mechanical properties [13–20]. Moreover, in all previous studies on P-containing steels, 0.2 at.% is almost the upper limit of the addition contents [19]. Exceeding this limit by adding P excessively would cause significant embrittlement in these steels [16,18,19]. Therefore, the selected level of P addition in this study is approximately 0.2 at.%.

Multiple-principal-element alloys, also referred as high-entropy alloys (HEAs) and medium-entropy alloys (MEAs) [23–25], have been a hot research topic and attracted extensive research interests in the last two decades due to their excellent mechanical and physical properties. Single-phase face-centered cubic (FCC) HEAs or MEAs, such as CrMnFeCoNi HEA [26] and CrCoNi MEA [27,28] have drawn special attention in the last decade due to their superior mechanical properties at room temperature and even better mechanical properties at cryogenic temperature. The dominant deformation mechanisms in these HEAs/MEAs have been found to transit from the dislocation slip at room temperature to the deformation twins at cryogenic temperature [29]. However, the yield strength of these single-phase FCC HEAs/MEAs with coarse grains is still low, limiting their practical applications. For this purpose, interstitial solution strengthening with C and N was applied to the CrCoNi MEA [12,30], while a loss in ductility was also observed. In this regard, a P-doped CrCoNi MEA with the addition of a small amount of P element (0.2% P, at.%) has been developed for the first time in this study. Both yield strength and uniform elongation were observed to be simultaneously improved in the P-doped CrCoNi MEA, as compared to the un-doped CrCoNi MEA. Then, the corresponding strengthening and hardening mechanisms due to the P addition were revealed by detailed microstructure characterizations.

2. Experimental

2.1. Materials and processing

The chemical compositions of the P-doped CrCoNi MEA and the un-doped CrCoNi MEA are $Cr_{30.64}Co_{32.95}Ni_{36.21}P_{0.2}$ and $Cr_{32.46}Co_{33.48}Ni_{34.06}$ (in at.%). The raw materials were melted first by electromagnetic levitation under protection of high-purity argon for several times to reach chemical homogeneity, and then cast into about 10 kg of ingots. The ingots were homogenized at 1473 K for 12 h, hot-forged to 20 mm thick plates at 1373 K initial temperature, then hot-rolled to 10 mm thick at 973 K temperature, and finally cold-rolled to 1 mm sheet. After cold rolling, P-doped CrCoNi MEAs were annealed at 1273 and 1423 K for 2 h, and un-doped CrCoNi MEAs were annealed at 1273 and 1373 K for 1 h, followed by water quenching. These specimens are referred as CrCoNi-P-FG, CrCoNi-P-CG, CrCoNi-FG, and CrCoNi-CG, hereafter.

2.2. Testing methods of mechanical properties

The quasi-static uniaxial testing and load-unload-reload (LUR) testing were conducted utilizing an Instron 5565 testing machine at room temperature and a strain rate of 5×10^{-4} s^{-1}. The dimensions of the gauge section for the tensile dog-bone shaped specimens are 10 mm×2 mm×1 mm. Five repeated tests were conducted for each sample to ensure the data repeatability and provide the error bar. In the LUR test, the specimen was stretched to the specified strain, then unloaded at an unloading rate of 200 N/min to 20 N, and then reloaded. In tensile tests and LUR tests, a extensometer was used to accurately measure and control displacement. The other details for the LUR tests can be found in our previous research [31,32]. All specimens used for tensile testing are mechanically polished to eliminate surface irregularities and ensure a more accurate determination of the cross-sectional area.

2.3. Microstructure characterization

X-ray diffraction (XRD) was used to analyze the phase composition of P-doped CrCoNi MEAs and un-doped CrCoNi MEAs. XRD scanning ranges from 20° to 100°, step size is 0.01°, and scanning speed is 2°/min. A Zeiss Gemini SEM 300 scanning electron microscope (SEM) equipped with an electron backscatter diffraction (EBSD) system from Oxford and a 200 kV high-resolution projection electron microscope (HR-TEM, JEOL 2100F) were used to characterize the microstructures prior to and after tensile testing. For EBSD acquisition, two types of mapping were performed using lower and higher magnifications with step sizes of 0.2 and 0.03 μm for global and detailed microstructural analysis, respectively. High-angle grain boundaries (HAGBs) and low-angle grain boundaries (LAGBs) in this study were defined as grain boundaries with misorientation angles >15° and in the range of 2°-15°, respectively. Σ3 twin boundaries (TBs) were automatically recognized by a fully automatic EBSD analysis system (TSL OIM Data Collection 5 Software) with the misorientation of 60°±2°. Due to the spatial resolution of the EBSD system, the misorientations of less than 2° were not identified. The grain size was measured by the volume-equivalent grain diameter method and EBSD examinations, according to the procedures given in ASTM E1382. In this work, the grain size was measured without considering annealing TBs.

Samples for both XRD and EBSD tests were polished and thin sheets for TEM observations were grounded to 35 μm thick and finally thinned by double-jet polishing with a solution of 10% perchloric acid and 90% ethanol at -25°C with a potential of 38 V.

The distribution of elements around the grain boundaries was determined using local electrode atom probe tomography (APT, CAMECA LEAP 5000 XR). APT samples were prepared under a focused ion beam/scanning electron microscope (FIB/SEM, Helios Nanolab G3). In voltage pulse mode, the APT sample was analyzed at 50 K with a repetition rate of 200 kHz and a pulse fraction of 20%. Imago Visualization and Analysis Software (IVAS) 3.8.2 were used to reconstruct and analyze APT data. The other details about these methods and the specimen preparation can be found elsewhere [33].

3. Results

The inverse pole figures (IPF) by EBSD observations for two selected samples (CrCoNi-FG and CrCoNi-P-FG) before tensile tests are presented in Fig. 1(a) and (b), in which only HAGBs and twin boundaries are shown. In order to minimize the effects of other structural factors (such as grain size) on the tensile properties of the alloys, the average grain sizes of the present alloy and the reference alloy were set to be similar through different heat treatment modifications. The CrCoNi-FG and CrCoNi-P-FG samples are observed to consist of equiaxed grains, and the average grain sizes for these samples are 39 and 42 μm, respectively. Numerous annealing twins can also be found in these two samples. The average grain sizes of the CrCoNi-CG and CrCoNi-P-CG samples are 120 and 110 μm respectively, and the corresponding EBSD images are not shown here for saving spaces.

In order to investigate any meaningful difference in the lattice constants of these two samples, the corresponding XRD measurements were conducted, and the results are displayed in Fig. 1(c).

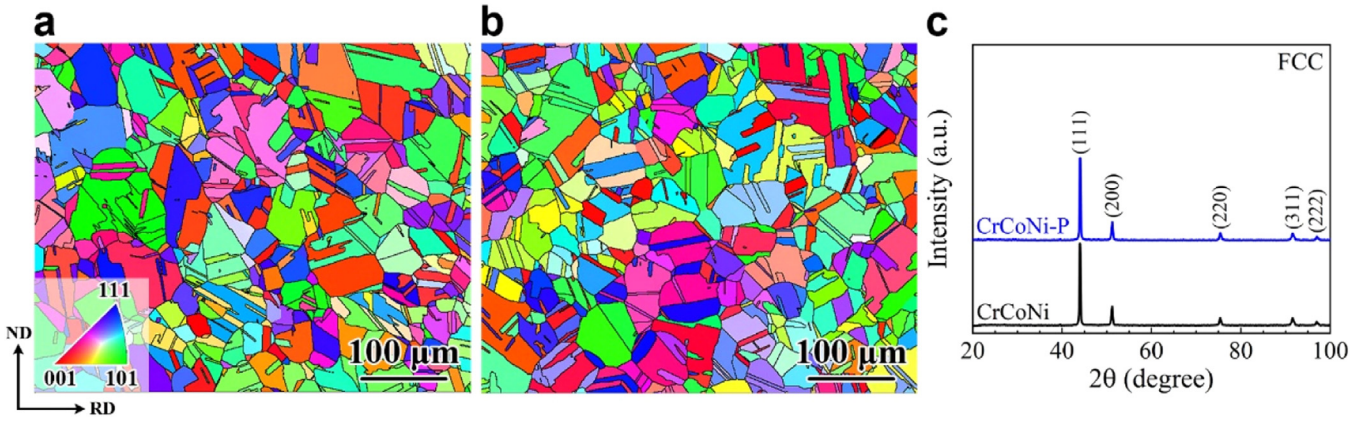

Fig. 1. IPF images prior to tensile testing for (a) the CrCoNi-FG sample and (b) the CrCoNi-P-FG sample. (c) The corresponding XRD spectra for the two samples.

Single-phase FCC structures were observed for both samples based on the XRD spectra, thus the P addition did not alter the crystal structure.

More importantly, it is indicated that the lattice constants of the two alloys are: $a_{CrCoNi-P}$= 0.3577 nm, and a_{CrCoNi}=0.3580 nm, respectively. The reason for the decrease in lattice constant by P addition may be attributed to its role as a substitutional solute with a smaller atomic radius. Solid-solution element additions can cause changes in lattice constants and lattice distortions, which affect dislocation behavior and macroscopic mechanical properties in M/HEAs [34].

TEM and HR-TEM images for the CrCoNi-P-FG sample prior to tensile testing are given in Fig. 2(a) and (b). Several straight GBs can be clearly observed. Moreover, nearly no dislocations can be observed inside the grain interiors, which can be due to the high-temperature annealing. Near-atomic level chemical element distributions across two grains are revealed by 3D-APT, and the results are shown in Fig. 2(c) and (d). The Cr, Co, and Ni elements are observed to have nearly equal atomic ratios, and the distributions of these elements are homogeneous. However, the distribution of P element is found to be inhomogeneous. The P element exist in two different forms in the CrCoNi-P-FG sample: one is forming solute atoms inside the grain interiors, and the other is generating P segregation at GBs. Analysis of the 1D concentration profile reveals that the content of P element as solute atoms within the matrix (excluding GBs) is 0.08±0.04 at.% (Fig. 2(d)). It can be seen that the concentration of P atoms inside the grain interiors is considerable, and it also exhibits certain fluctuations in concentration. Therefore, such P distribution inside the grain interiors affects not only the overall average stacking fault energy (SFE) but also the atomically local SFE, which is consistent with model predictions in the previous research [35]. Meanwhile, the P-segregation micro-domains at GBs are marked by a 0.6 at.% P iso-concentration surface. Such P segregation at GBs can reduce the activation energy of GB migration, inhibiting grain growth and stabilizing grains [36,37]. It can be inferred that the existence of both forms of P atoms in the present alloy should have a significant impact on its deformation behavior and mechanical properties.

HR-TEM images showing detailed information of extended dislocations and stacking faults (SFs) for the CrCoNi-P-FG sample prior to tensile testing are displayed in Fig. 3. A few of extended dislocations can be observed in the annealed state, as indicated in Fig. 3(a). The corresponding diffraction pattern through fast Fourier transformation (FFT) is also given in the inset of Fig. 3(a), clearly indicating the existence of SFs by streaks (marked by a pair of arrowheads). An extended dislocation, with leading and trailing partials separated by an SF, is clearly shown in Fig. 3(b). In general, both repulsive and attractive forces exist between two partials in the extended dislocations. The repulsive force is exerted by the interaction of two partials themselves, while the attractive force originates from the SF. In a thermal-balanced state (such as the fully annealed state in the present study), these two forces are in balance, then the SFE can be calculated based on the following equation [38–40]:

$$\mathrm{SFE} = \frac{Gb^2}{8\pi d}\left(\frac{2-\nu}{1-\nu}\right)\left(1-\frac{2\nu\cos(2\beta)}{2-\nu}\right), \quad (1)$$

where G is shear modulus (87 GPa [41]), ν is the Poisson's ratio (0.3 [39]), b is the Burgers vector of partial dislocations (0.146 nm [39]), β is the angle between line direction of the un-dissociated dislocations and the Burgers vector (0°), and d is the separation width of two partials (SF width is measured by numerous extended dislocations). More than fifteen SFs were measured and analyzed by utilizing the HR-TEM technique along <011> zone axis, and the corresponding statistical results indicate that the average SF width is 9.67 ± 2.37 nm. The calculated SFE at room temperature for the P-doped CrCoNi MEA is 12.5 ± 2.5 mJ/m^2, which is much lower than that of the CrCoNi MEA (22 ± 4 mJ/m^2) [39]. Apparently, a much lower SFE is obtained by the addition of a small amount of P element. The HR-TEM images related to the SFE measurement, as well as the statistical results of the SF width, can be found in Supplementary Information.

The tensile properties for the un-doped and doped CrCoNi MEAs are compared and displayed in Fig. 4. Two samples for the un-doped CrCoNi MEA and the doped CrCoNi MEA were tested, and the grain sizes were chosen to be similar (39 μm vs. 42 μm; 120 μm vs. 110 μm). In this way, the only effect of P doping can be studied, excluding the grain size effect. Engineering stress-strain curves are shown in Fig. 4(a), while the true stress and hardening rate as a function of true strain for two selected samples (CrCoNi-FG and CrCoNi-P-CG) are given in Fig. 4(b) and (c), respectively. It is clearly observed that both yield strength and uniform elongation are simultaneously improved in the doped CrCoNi MEA at two levels of grain size, as compared to those in the un-doped CrCoNi MEA. Moreover, a transient up-turn phenomenon for hardening rate is found in both samples, and this up-turn phenomenon generally can be attributed to the heterogeneous structures, the TRIP effect, twinning-induced- plasticity (TWIP) effect and formation of SFs [28,42–44]. Interestingly, the doped CrCoNi MEA shows a higher hardening rate at the whole strain range, as compared to the un-doped CrCoNi MEA. The tensile properties of uniform elongation (ε_u) vs. yield strength (σ_y) for the P-doped CrCoNi MEA, along with literature data for the CrCoNi MEA [3–5,9,27,28,45,46], the CrCoNi-N MEA [12,15,47] and the CrCoNi-C MEA [30,48,49], are summarized in Fig. 4(d). The P-doped CrCoNi MEA shows a better

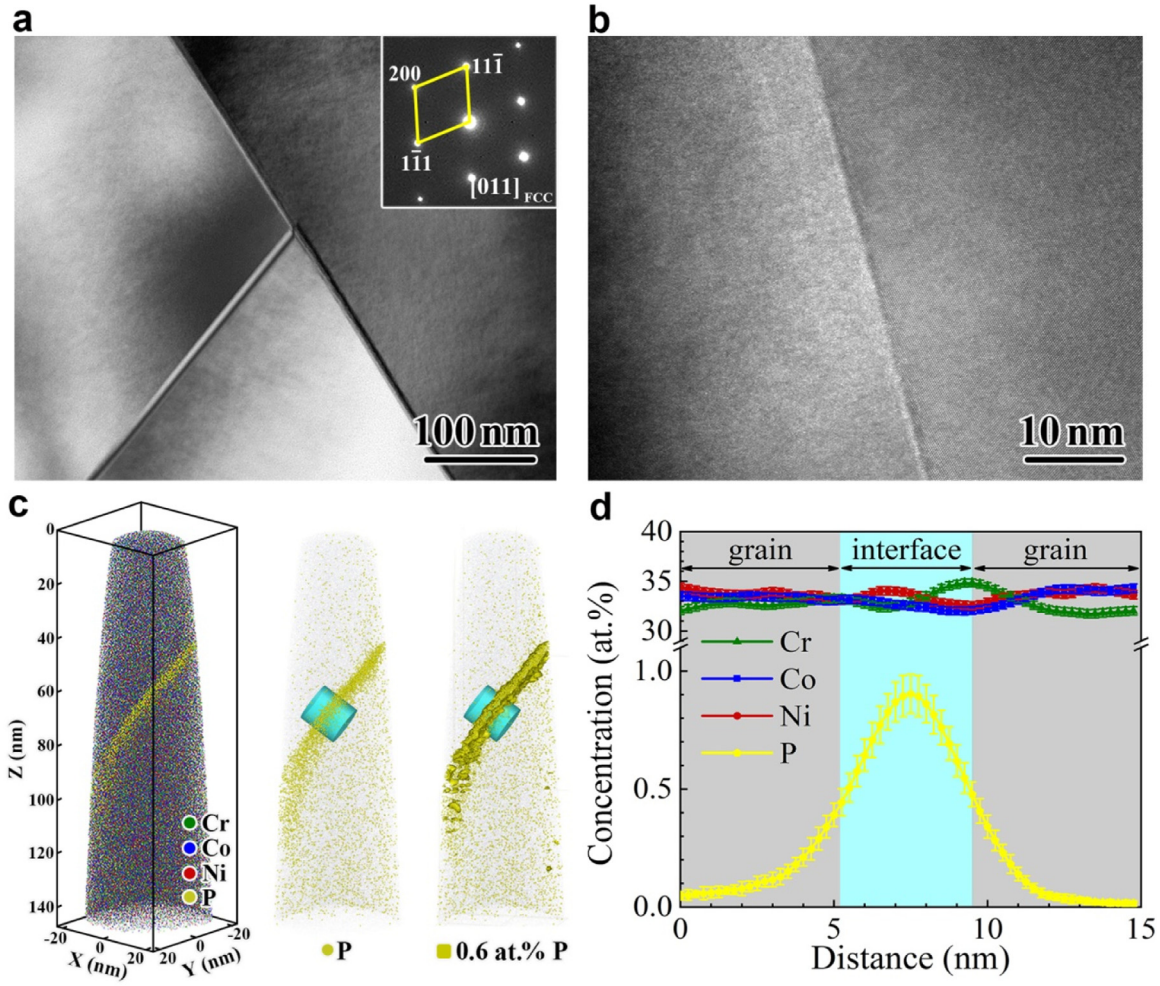

Fig. 2. (a, b) TEM and HR-TEM images of the CrCoNi-P-FG sample before tensile test. (c) 3D-APT mapping of overall atoms and individual P-atoms, as well as the reconstruction of the 0.6 at.% P iso-concentration surface. (d) 1D concentration profile for near-atomic level chemical element distributions across the GB.

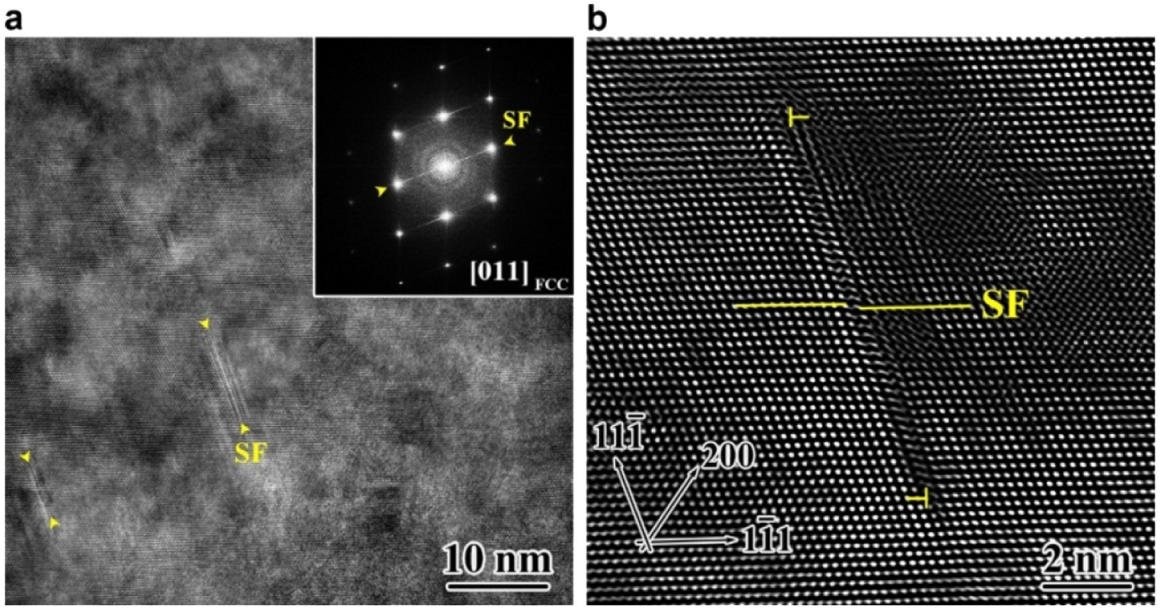

Fig. 3. (a) HR-TEM image of the SFs in the CrCoNi-P-FG sample prior to tensile testing. The diffraction pattern after FFT is given in the inset, showing the presence of SFs by streaks (marked by a pair of arrowheads). (b) Dislocation dissociation. The width between the two partials is about 9.7 nm.

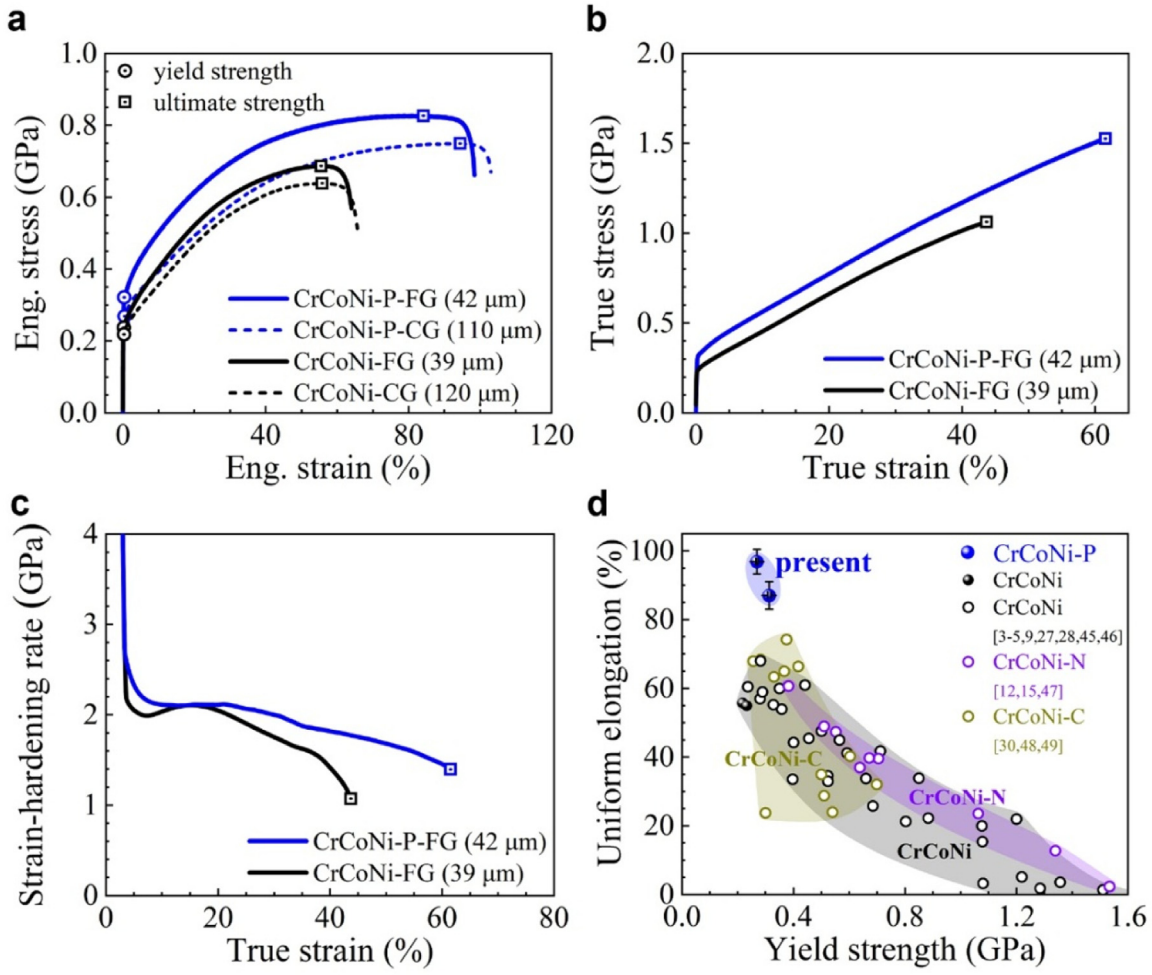

Fig. 4. Tensile properties for the un-doped CrCoNi and P-doped CrCoNi MEAs. (a) Engineering stress-strain curves. (b) True stress and (c) hardening rate (c) as a function of true strain. (d) Uniform elongation (ε_u) vs. yield strength (σ_y) for the P-doped CrCoNi MEAs, along with literature data for the CrCoNi MEA [3–5,9,27,28,45,46], the CrCoNi-N MEA [12,15,47] and the CrCoNi-C MEA [30,48,49].

strength-ductility synergy compared to the un-doped CrCoNi MEA. The P-doped CrCoNi MEA also displays significantly larger tensile ductility at similar yield strength levels than the other-element-doped CrCoNi MEAs.

It is well known that the dominant deformation mechanisms for the CrCoNi MEA are the deformation twins [27,28,39,50]. Deformation twins can induce microstructure refinement in the grain interiors, and such microstructure refinement can result in the reduction of dislocation mean free path and the so-called dynamic Hall-Petch effect [9,39]. Heterogeneity in microstructures can be induced by the formation of deformation twins during tensile deformation. Thus, the kinematic and hetero-deformation-induced (HDI) hardening should play an important role in the plastic deformation of metals and alloys with TWIP effect [5,28,42]. For the P-doped CrCoNi MEA, the HDI hardening might also be important due to the microstructure refinement by the other possible defects. In this regard, LUR tests were conducted on one typical un-doped sample (CrCoNi-FG sample) and one typical doped sample (CrCoNi-P-FG sample) in order to study and compare their HDI hardening effects. The true stress-strain curves for LUR tests are displayed in Fig. 5(a), and the typical hysteresis loops at one predetermined tensile strain are shown in Fig. 5(b). The HDI stress can be estimated based on the un-loading and re-loading yield stresses, and the calculation method can be found in our previous research [31,32]. Then, the HDI stress (σ_{HDI}) and the HDI hardening contribution ($\sigma_{HDI}/\sigma_{flow}$) are plotted as a function of true strain in the Fig. 5(c) and (d), respectively. It is clearly seen that the P-doped CrCoNi MEA shows higher HDI stress and higher HDI hardening contribution, as compared to the un-doped CrCoNi MEA. The origins of higher HDI hardening effect in the P-doped CrCoNi MEAs will be discussed next.

The deformation mechanisms for a typical sample of the P-doped CrCoNi MEA (CrCoNi-P-FG) were characterized by EBSD first. Microstructure evolution (as revealed by IPF images) at varying tensile strains for the CrCoNi-P-FG sample is displayed in Fig. 6(a–h). Image quality (IQ) figures with various boundaries (high-angle grain boundaries, low-angle grain boundaries, and Σ3 twin boundaries) at tensile strains of 20%, 30%, 70% and 90% are given in Fig. 6(e1–h1). At large tensile strains, the equiaxed grains are observed to be severely deformed. Deformation twins are not observed until the tensile engineering strain reaches about 30%. Based on the EBSD observations, we can assume that the initiation stage for deformation twins can be defined at the true strain range of 26%-41%. Based on the true stress-strain curve for the CrCoNi-P-FG sample, the critical stress for nucleation of deformation twins in the P-doped CrCoNi MEA can be estimated to be 1050 ± 150 MPa, which is much higher than that for the CrCoNi MEA (790 ± 100 MPa) [39]. Thus, the addition of P element can elevate the critical stress for nucleation of deformation twins, and deformation twins are delayed and depressed in the P-doped CrCoNi MEA.

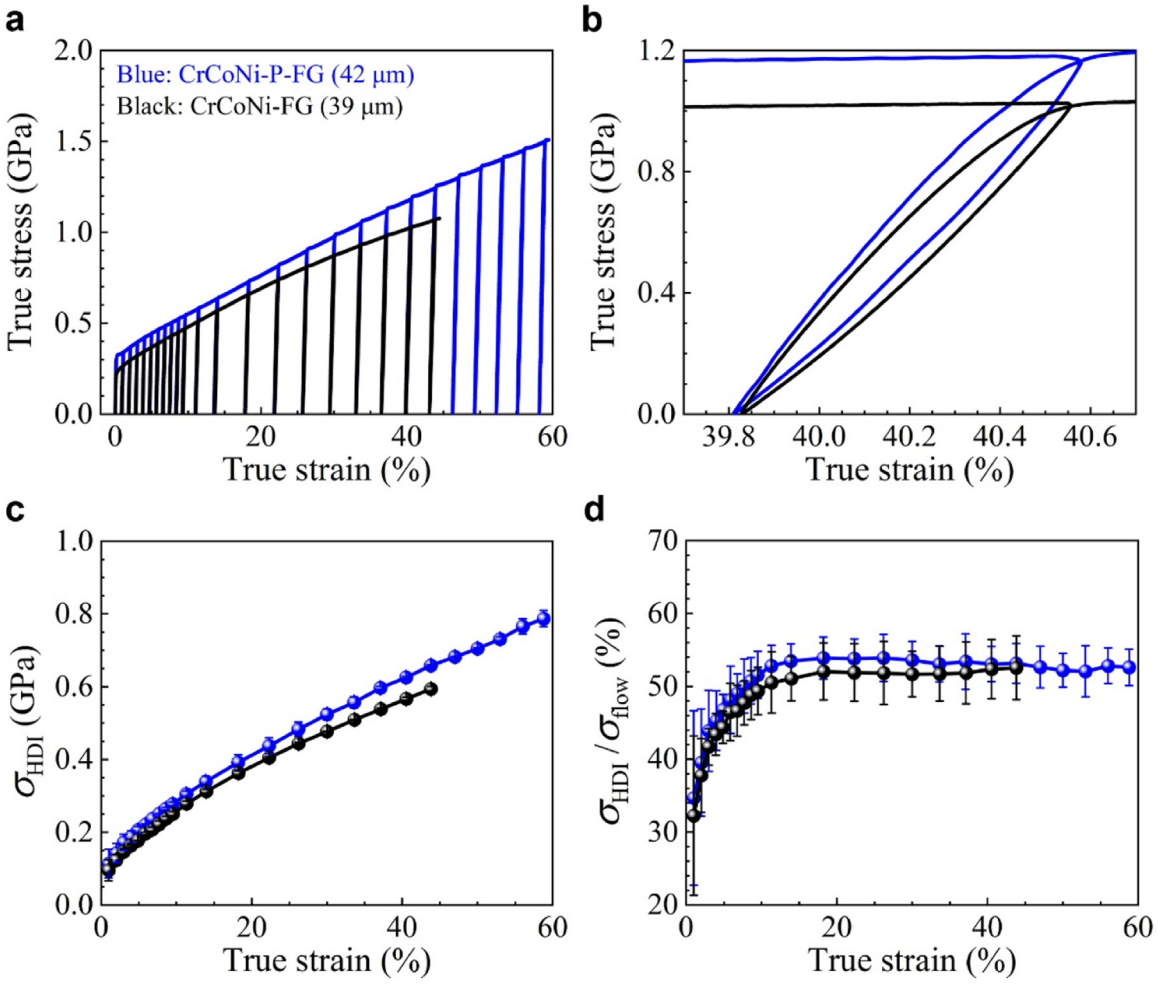

Fig. 5. HDI hardening for one typical un-doped sample and one typical doped sample. (a) True stress-strain curves for LUR tests. (b) Typical hysteresis loops at one predetermined tensile strain. (c) Plots of σ_{HDI} as a function of true strain. (d) Plots of the ratio of HDI stress and flow stress ($(\sigma_{HDI}/\sigma_{flow})$ as a function of true strain.

Moreover, the corresponding critical shear stress values for twinning initiation in both P-doped and P-free alloys were calculated. According to the Taylor hardening model, the increase in shear stress ($\Delta\tau$) due to forest dislocation interactions is given by [51]:

$$\Delta\tau = \Delta\sigma/M \tag{2}$$

where $\Delta\sigma$ is the corresponding increase in the tensile stress, M is the Taylor factor (3.06).

The true tensile stress and resolved shear stress for the onset of twinning for the CrCoNi-P MEA are 1050±150 and 345±50 MPa, respectively; for the CrCoNi MEA are 790±100 and 260±30 MPa, respectively [39]. According to previous research [51], these two values in the CrMnCoFeNi alloy are 720±30 and 235±10 MPa, respectively. It can be observed that, as compared to the CrCoNi and CrMnCoFeNi alloys (with SFEs of 22 and 30 mJ/m^2, respectively), the critical shear stress of the CrCoNi-P MEA (345±50 MPa) is increased by 33% and 47%, respectively. Similar experimental results have been reported in other M/HEAs [34,52,53].

The KAM maps at varying tensile strains (1%, 2%, 5%, 10%, 20%, 30%, 70% and 90%) for the CrCoNi-P-FG sample are displayed in Fig. 7. It is well known that the KAM value can reflect the GND density based on the strain-gradient theory [54]. The average GND density is observed to increase with increasing tensile strain. It also can be seen that GNDs appear first at grain boundaries at tensile strains of 10%, 20% and 30%, and then spread out to the grain interiors and the whole sample at larger tensile strains (70% and 90%). It can be concluded that deformability among grains is different and strain partitioning exists between different grains. The grain boundaries are the dominant factors controlling the plastic deformation accommodation among various grains. Thus, the higher strain gradients and GNDs appear first at grain boundaries for accommodating plastic deformation and sustaining large ductility.

The Schmid factor maps at varying tensile strains (1%, 10%, 30%, and 90%) for the CrCoNi-P-FG sample are shown in Fig. 8(a–d). The evolution of the Schmid factor distributions with increasing tensile strain is presented in Fig. 8(e). The average Schmid factor is found to decrease with increasing tensile strain, which can be attributed to plastic deformation. It was reported that single-peak distributions can be observed prior to and after tensile deformation for the FeCoNi MEA [55]. While, double-peak distributions for the Schmid factor are found for the P-doped CrCoNi MEA at varying tensile strains, which means that the plastic deformation occurs grain-to-grain and strain partitioning is observed among grains. This strain partitioning can cause the stress state change for various grains, and induce strain gradients at boundaries for HDI hardening.

The plastic deformation mechanisms for a typical sample of the P-doped CrCoNi MEAs (CrCoNi-P-FG) were also characterized by TEM. Bright-field TEM images for the CrCoNi-P-FG sample at varying tensile strains (1%, 10%, 30% and 90%) are shown in Fig. 9(a–d), while the corresponding close-up views are presented in Fig. 9(a1-

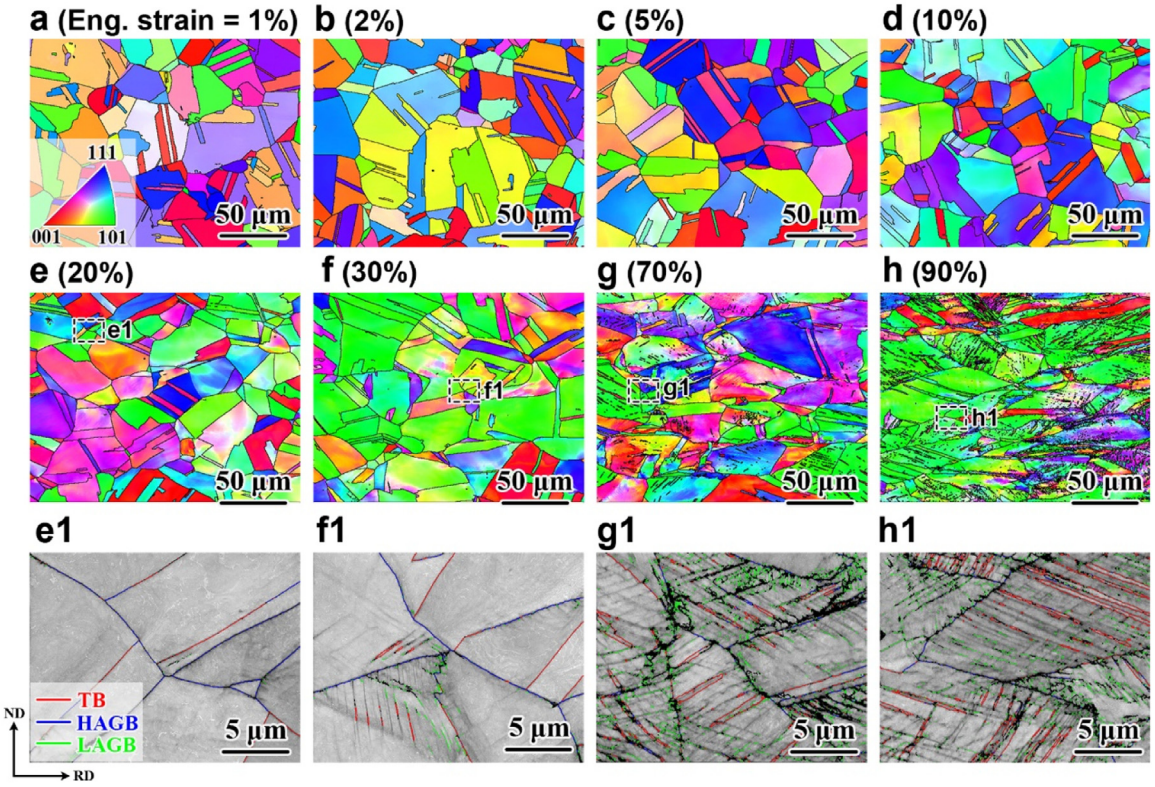

Fig. 6. Microstructure evolution during tensile deformation for the CrCoNi-P-FG sample. IPF images at tensile strains of (a) 1%; (b) 2%; (c) 5%; (d) 10%; (e) 20%; (f) 30%; (g) 70%; (h) 90%. IQ images with various boundaries at tensile strains of (e1) 20%; (f1) 30%; (g1) 70%; (h1) 90%.

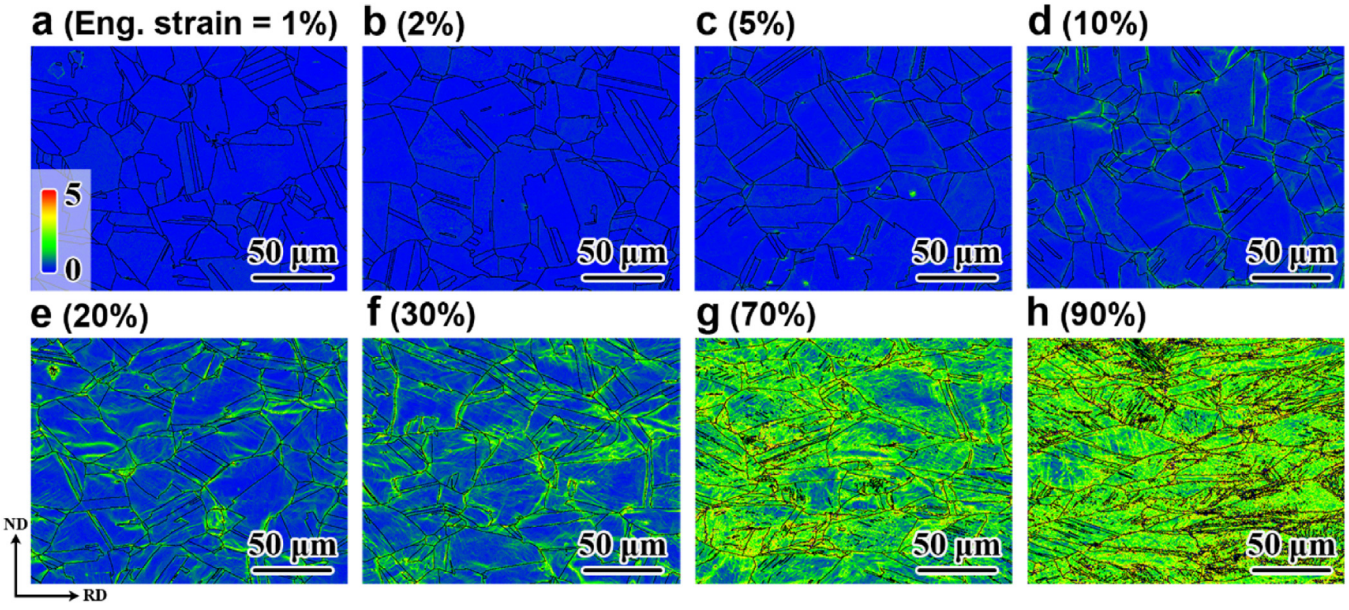

Fig. 7. Microstructure evolution during tensile deformation for the CrCoNi-P-FG sample. KAM maps at tensile strains of (a) 1%; (b) 2%; (c) 5%; (d) 10%; (e) 20%; (f) 30%; (g) 70%; (h) 90%. Scale bar is given in (a).

d1). At a tensile strain of 2%, planar dislocations are observed in Fig. 9(a), and most of them are from one slip system. While the density of planar SF interfaces increases in volume fraction with increasing tensile strain afterwards. SFs can be identified by the selected area electron diffraction (SAED) pattern in the insets of Fig. 9(b–d). For example, the formation of SFs is observed (most of them are also from one slip system) at a tensile strain of 20%, and the formed SFs can provide strong barriers for further dislocation slip, and this interaction between dislocations and SFs can provide strong hardening. More SFs from two slip systems can be observed, parallelograms intersected by SFs are formed at a tensile strain of 30%, and the spacing between SFs becomes smaller (several tens of nm). At a larger tensile strain of 90%, parallelepiped domains are formed with dense walls. The effects of these parallelepiped domains with dense walls on strain hardening are very similar to those for microband-induced-plasticity steels [56]. Such dynamic

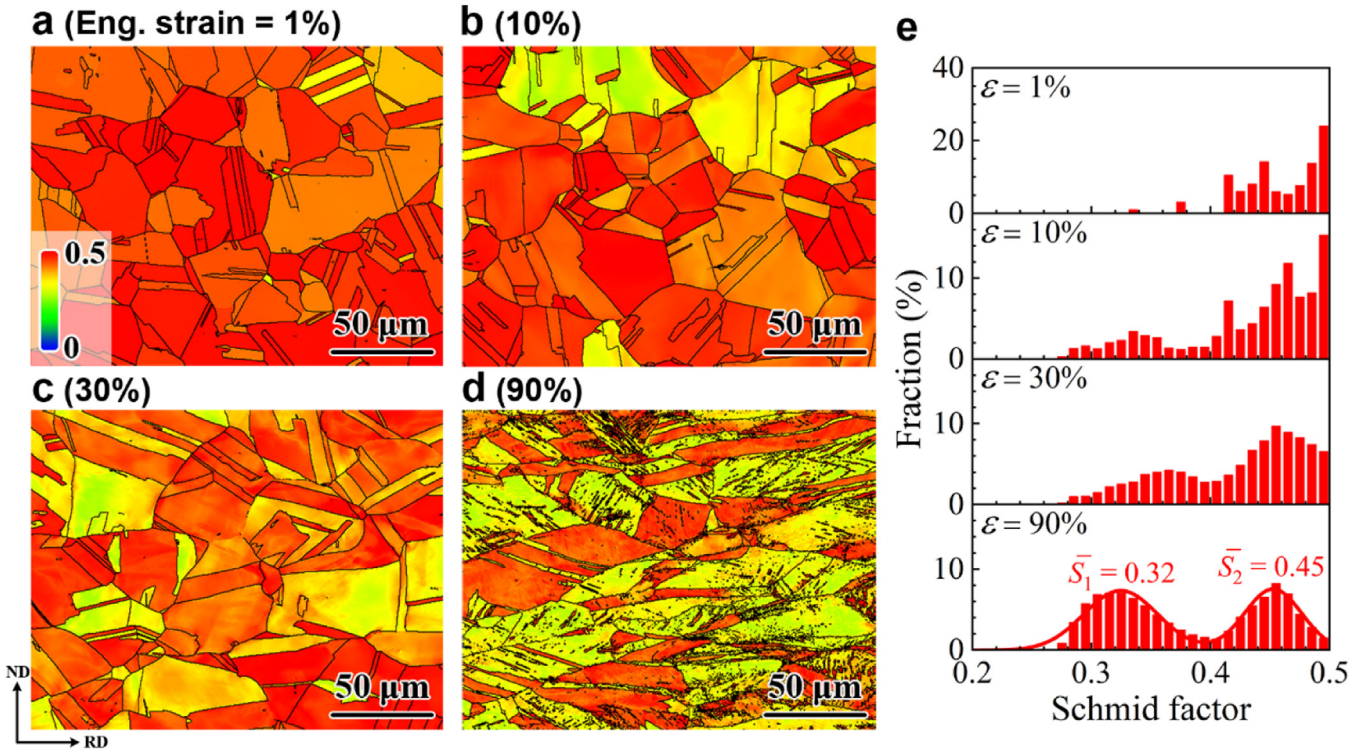

Fig. 8. Schmid factor maps for the CrCoNi-P-FG sample at tensile strains of (a) 1%; (b) 10%; (c) 30%; (d) 90%. Scale bar is given in (a). (e) Distributions of Schmid factor at various tensile strains.

structural refinement by SFs should also contribute significantly to the HDI hardening in the P-doped CrCoNi MEAs.

HR-TEM images for the CrCoNi-P-FG sample at varying tensile strains (30%, 70% and 90%) are presented in Fig. 10(a–f). The corresponding diffraction patterns acquired by FFT of the HR images are given in Fig. 10(a1–f1), clearly showing the existence of SFs. It can be observed that the domain boundaries for the parallelepiped domains in Fig. 9 actually consist of numerous SFs. Moreover, the density of SFs becomes higher and higher with increasing tensile strain. For example, the thickness for the domain boundaries at a tensile strain of 30% is about 5–10 nm, consisting of several SFs. While the thickness of the domain boundaries increases to several tens of nanometers, consisting of several tens of SFs. It also can be observed that a lot of SFs are formed inside these domains. The interactions of dislocations with these domain boundaries consisting of SFs should provide strong hardening, which can be so-called SF-induced plasticity [7,44,53,57].

4. Discussion

It is well known that solution strengthening plays an important role in the yield strength of HEAs/MEAs [8,11,15]. In general, interstitials, e.g., C, N, and O, are attractive small atoms for interstitial sites to create strong lattice distortions and hence strengthen metals and alloys significantly [11,14,15]. HEAs/MEAs, as multiple-principal-element alloys, can also induce severe lattice distortion themselves for strong solution strengthening [8]. For example, vanadium element was proven to be a crucial element in HEAs and MEAs, and ultra-high yield strength can be achieved by severe lattice distortion and solid-solution strengthening in V-based HEAs/MEAs, such as the VCoNi MEA [8], the $Al_xTi_y(VCoNi)_{(100-x-y)}$ MEAs [58]. Moreover, the chemical short-range ordering (CSRO) has also been shown to have a significant influence on the yield strength of HEAs/MEAs recently [59,60]. The effect of grain size on yield strength can be well predicted by the well-known Hall-Petch relationship, and the strengthening coefficient (k) has been found to be several times higher in HEAs/MEAs due to the lattice distortion and CSRO, as compared to the pure metals [8,59]. P element, as one of the strongest elements for substitutional solution strengthening in alloys [20], can increase the severity of lattice distortion on one hand, and can also elevate the degree of CSRO on the other hand in the CrCoNi MEA. Thus, the enhanced yield strength in the P-doped CrCoNi MEA with similar grain size and dislocation density can be attributed to the aforementioned two effects, as compared to the un-doped CrCoNi MEA.

Based on the microstructure evolutions by EBSD and TEM, the schematic of hardening mechanisms for the P-doped CrCoNi MEA can be summarized in Fig. 11. The initial microstructure can be considered as equiaxed grains with lots of annealing twins (Fig. 11(a)). At small tensile grains (<5%), the deformation mechanisms can be characterized as planar dislocation arrays in multiple slip systems (Fig. 11(b)). At larger tensile grains (~30%), the deformation mechanisms can be considered as SF networks and domains formed by SFs in multiple slip systems (Fig. 11(c)), and the domain size and the domain-boundary spacing are several tens of nm. Massive lamellar bundles with high density of SFs intersect each other at this stage, forming parallelepiped domains. At the ultimate strength point (~90%), more SFs are formed inside the parallelepiped domains, the thickness of domain boundaries and the overall SF density increase significantly (Fig. 11(d)). As indicated in Fig. 2, a peak distribution and element segregation for P are observed at grain boundaries, and such P segregation at grain boundaries can reduce the activation energy for grain boundary migration, stabilize grains and promote dislocation behaviors. Moreover, a much lower SFE can be obtained in the P-doped CrCoNi MEA as compared to the un-doped CrCoNi MEA (12.5 mJ/m^2 vs. 22 mJ/m^2, Fig. 3).

Recently, there has been a wealth of literature on the microstructural evolution of the conventional CrCoNi MEA during tensile deformation, including not only the microstructural char-

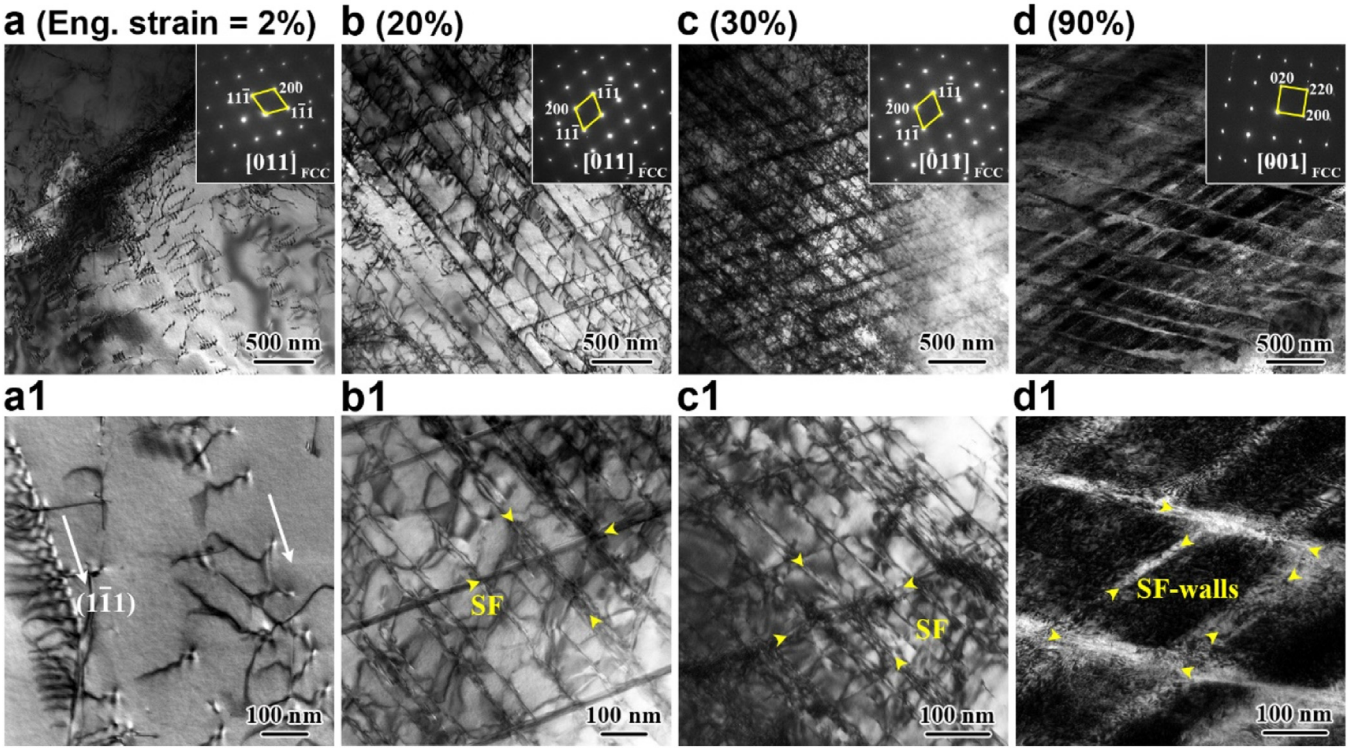

Fig. 9. Bright-field TEM images for the CrCoNi-P-FG sample at tensile strains of (a) 1%; (b) 20%; (c) 30%; (d) 90%. The corresponding close-up views are presented in (a1–d1). The SFs and high-density SF walls are indicated by yellow arrowheads.

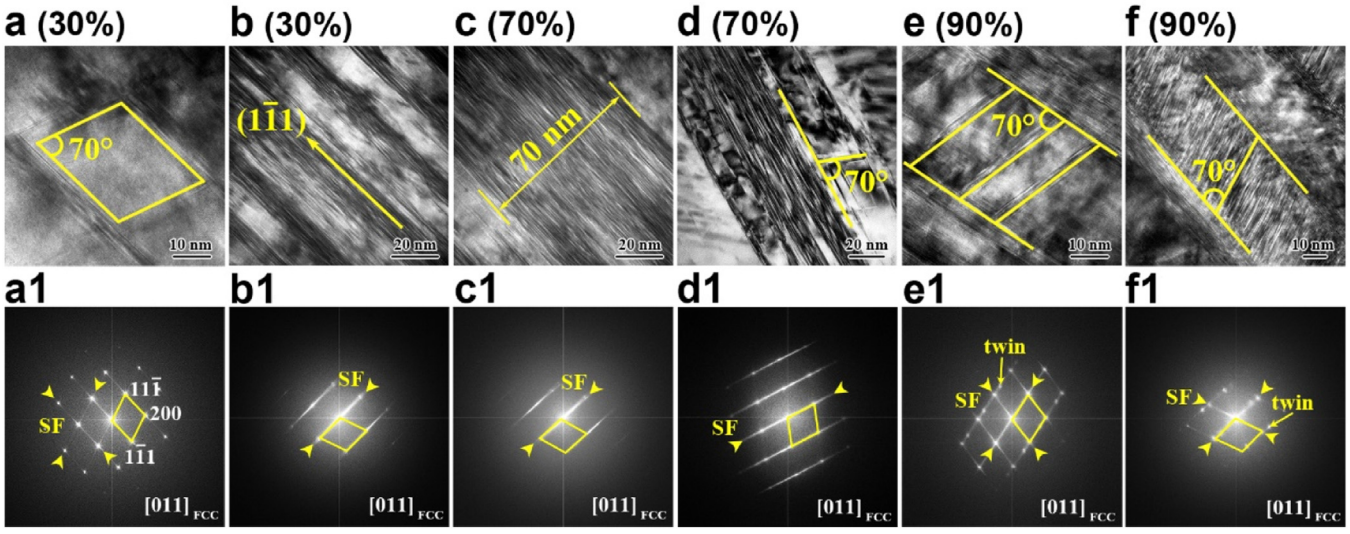

Fig. 10. HR-TEM images for the CrCoNi-P-FG sample at tensile strains of (a, b) 30%; (c, d) 70%; (e, f) 90%. The corresponding diffraction patterns acquired by FFT of the HR-TEM images are presented in (a1–f1).

acteristics at various plastic strain stages [12,39], but also the evolution of deformation microstructures with different average grain sizes [39,48]. In general, plastic deformation in the CrCoNi MEA with average grain sizes between ~2 and 150 μm is dominated by deformation twinning at medium/large-strain levels during tensile deformation [12,39,48].

In contrast, the present CrCoNi-P MEA has a significant difference in the evolution pattern of the deformation microstructure (Figs. 6(e1–h1), 9 and 10), where the deformation twinning of the CrCoNi-P MEA is significantly suppressed and prolonged as compared to the reference CrCoNi MEAs [12,39,48,53,61–63]. For example, the trigger strain for {110}<1$\bar{1}$1> twinning in the CrCoNi-P MEA exceeds 30% (Figs. 9 and 10), whereas that in the reference CrCoNi MEAs is only in the range of 10%–14% [39,48,61]. Meanwhile, the deformation twinning persists in CrCoNi-P MEA over a broader applied strain range (i.e., 30% to 90%, see Figs. 6(f1–h1) and 10). These results indicate that deformation twinning in the present CrCoNi-P MEA is significantly delayed and sustained.

Furthermore, even upon straining to approximately 70%–90%, the twinning density in the CrCoNi-P MEA is considerably lower than the corresponding SF density (Figs. 9 and 10). In contrast, the proportions of high-density deformation twins in the reference CrCoNi MEAs deformed by approximately 30%–60% are significantly higher than that of the deformation SFs [39,48,61,62]. The defor-

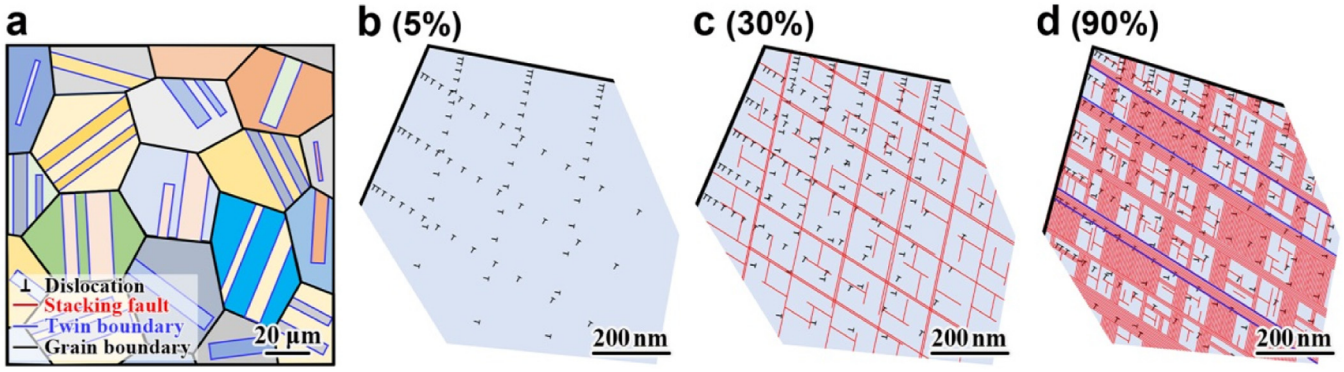

Fig. 11. Schematic illustration of the microstructural evolution of P-doped CrCoNi MEA during strain hardening under tension. (a–d) Upon tensile straining from 0 (no tension at all) to 90% (uniform elongation).

mation mechanism of the current P-doped CrCoNi MEA during tensile deformation is primarily controlled by SFs rather than deformation twinning.

These above-mentioned significant differences in the microscopic deformation mechanisms are what give the CrCoNi-P alloy its extra strain-hardening capacity (see Fig. 4(c)) and resulting strength-ductility synergy (Fig. 4(a)) at room temperature.

It's well-known that the modification of SFE by alloying can alter the plastic deformation mechanisms in medium-/low-SFE alloys, thereby influencing their macroscopic mechanical properties. It is widely accepted that when the SFE drops below a certain critical value, such as 20–40 mJ/m^2 for high-Mn steels [64,65], a transition in deformation mechanism occurs. This transition may involve phase transformation and deformation twinning [64,65]. The former is not detected at any plastic strain in the present alloy, while the latter is only observed when plastic strain reaches 30%. The decreasing SFE should enhance the twinning propensity in general. However, the current experimental observations reveal the opposite effect. Specifically, with P addition leading to a 43% reduction in SFE (from 22 mJ/m^2 down to 12.5 mJ/m^2), twinning initiation is delayed, and deformation twinning occurs roughly at plastic strains between 30% and 90% (Figs. 6 and 9). We are not very clear at the moment about the nature behind this contradictory phenomenon, however, it can be conjectured that the distribution of local SFE might be more inhomogeneous in the CrCoNi-P MEA due to the addition of P and the element distribution fluctuations [35]. Therefore, a weaker tendency for twinning in the present alloy could be attributed to the possible more inhomogeneous distribution of SFE. Further clarification is required to understand the corresponding microscopic mechanisms for the weaker twinning propensity in the CrCoNi-P MEA in the future.

As reported in previous literature, in comparison with the CrMnCoFeNi HEA (γ_{SF} = 30 mJ/m^2; τ_c= 720±30 MPa), the CrCoNi alloy with relatively lower SFE (γ_{SF} = 22 mJ/m^2) instead exhibits a higher critical tensile stress for twinning (τ_c = 790±100 MPa). The phenomenon of simultaneously possessing low SFE and high critical twinning stress has also been reported in Cu-Al alloys [66], and H/MEAs [13,34,53].

Traditional strengthening mechanisms invariably induce a strength-ductility dilemma, they strongly resist dislocation movement for strengthening while also greatly reducing the dislocation accumulation in structures with small size for diminished strain hardening. However, plentiful multi-orientational tiny planar SFs induce dynamic structural refinement for forming parallelepiped domains in the present P-doped CrCoNi MEA. These nano-sized domains with domain boundary spacing at tens of nm can block dislocation slip for strengthening on one hand, and can accumulate SFs and dislocations in the interiors of domains for exceptionally high strain hardening rate for the P-doped CrCoNi MEA on the other hand.

5. Conclusions

In the present study, an addition of small amount of P element (0.2 at.%) was applied to form a P-doped CrCoNi MEA for the first time. And then, the tensile properties and the corresponding strengthening/hardening mechanisms were studied and compared for both the P-doped CrCoNi MEA and the un-doped CrCoNi MEA. The findings can be summarized as follows:

(1) The distribution of P element shows a peak at grain boundaries, such P segregation at grain boundaries can reduce grain boundary energy, stabilize grains for elevating yield strength and promote dislocation behaviors. Moreover, a much lower SFE can be obtained in the P-doped CrCoNi MEA as compared to the un-doped CrCoNi MEA (12.5 mJ/m^2 vs. 22 mJ/m^2).
(2) Both yield strength and uniform elongation are observed to be simultaneously improved in the P-doped CrCoNi MEA, as compared to the un-doped CrCoNi MEA. Moreover, the P-doped CrCoNi MEA also shows much larger tensile ductility at a similar yield strength level, as compared to the other-element-doped CrCoNi MEAs.
(3) The P-doped CrCoNi MEA is observed to show higher HDI stress and higher HDI hardening rate, as compared to the un-doped CrCoNi MEA. A double-peak distribution for the Schmid factor and a first appearance for GNDs at grain boundaries are found for the P-doped CrCoNi MEA at varying tensile strains, indicating the grain-to-grain plastic deformation and strain partitioning for HDI hardening.
(4) The enhanced yield strength in the P-doped CrCoNi MEA can be attributed to the strong substitutional solution strengthening and GB segregation induced strengthening. Partial dislocations and SFs dominate over deformation twins due to the possible more inhomogeneous distribution of local SFE. Multi-orientational planar SFs refine structures, forming nano-sized domains blocking dislocation slipping, and accumulating SFs and dislocations in the interiors of domains for exceptionally high strain hardening rate. These insights aid in achieving superior tensile properties in H/MEAs through solution strengthening.

Data availability

The raw/processed data required to reproduce these findings cannot be shared at this time due to technical or time limitations.

Declaration of competing interest

The authors declare that they have no known competing financial interests or personal relationships that could have appeared to influence the work reported in this paper.

CRediT authorship contribution statement

Hangzhou Zhang: Writing – original draft, Validation, Investigation, Data curation. **Guoqiang Sun:** Resources, Investigation. **Muxin Yang:** Writing – review & editing, Supervision, Investigation, Funding acquisition, Conceptualization. **Fuping Yuan:** Writing – review & editing, Validation, Funding acquisition. **Xiaolei Wu:** Supervision, Project administration, Funding acquisition.

Acknowledgements

We thank Ms. Beibei Xu and Mr. Yulai Zhu, both affiliated with the Shanghai Institute of Microsystem and Information Technology (SIMIT), Chinese Academy of Sciences, for conducting the 3D-APT and FIB experiments. This research was financially supported by the National Key R&D Program of China (No. 2019YFA0209902), the Natural Science Foundation of China (Nos. 52071326, 52192593, and 51601204), the NSFC Basic Science Center Program for Multiscale Problems in Nonlinear Mechanics (No. 11988102), and the Strategic Priority Research Program of the Chinese Academy of Sciences (No. XDB22040503).

Supplementary materials

Supplementary material associated with this article can be found, in the online version, at doi:10.1016/j.jmst.2024.05.020.

References

[1] Y.P. Lu, X.Z. Gao, L. Jiang, Z.N. Chen, T.M. Wang, Jin.C. Jie, H.J. Kang, Y.B. Zhang, S. Guo, H.H. Ruan, Y.H. Zhao, Z.Q. Cao, T.J. Li, Acta Mater. 124 (2017) 143–150.
[2] T. Yang, Y.L. Zhao, Y. Tong, Z.B. Jiao, J. Wei, J.X. Cai, X.D. Han, D. Chen, A. Hu, J.J. Kai, K. Lu, Y. Liu, C.T. Liu, Science 362 (2018) 933–937.
[3] H. Huang, J.Y. Wang, H.L. Yang, S.X. Ji, H.L. Yu, Z.L. Liu, Scr. Mater. 188 (2020) 216–221.
[4] S. Yoshida, T. Bhattacharjee, Y. Bai, N. Tsuji, Scr. Mater. 134 (2017) 33–36.
[5] F.J. Guo, Y.F. Wang, M.S. Wang, W. Wei, Q. He, Q.Y. Wang, C.X. Huang, R.R. Jin, Scr. Mater. 218 (2022) 114808.
[6] J.Y. He, H. Bei, H.L. Huang, X.D. Xu, M.W. Chen, Y. Wu, X.J. Liu, T.G. Nieh, K. An, Z.P. Lu, Acta Mater. 102 (2016) 187–196.
[7] P.F. Wu, Y. Zhang, L.L. Han, K.F. Gan, D.S. Yan, W.S. Wu, L.H. He, Z.H. Fu, Z.M. Li, Acta Mater. 261 (2023) 119389.
[8] S.S. Sohn, A. Kwiatkowski Da Silva, Y. Ikeda, F. Körmann, W.J. Lu, W.S. Choi, B. Gault, D. Ponge, J. Neugebauer, D. Raabe, Adv. Mater. 31 (2019) 1807142.
[9] C.E. Slone, J. Miao, E.P. George, M.J. Mills, Acta Mater. 165 (2019) 496–507.
[10] G. Park, C.H. Nam, A. Zargaran, N.J. Kim, Scr. Mater. 165 (2019) 68–72.
[11] Z.M. Li, Acta Mater. 164 (2019) 400–412.
[12] I. Moravcik, H. Hadraba, L.L. Li, I. Dlouhy, D. Raabe, Z.M. Li, Scr. Mater. 178 (2020) 391–397.
[13] Z.W. Wang, I. Baker, Z.H. Cai, S. Chen, J.D. Poplawsky, W. Guo, Acta Mater. 120 (2016) 228–239.
[14] Z.F. Lei, X.J. Liu, Y. Wu, H. Wang, S.H. Jiang, S.D. Wang, X.D. Hui, Y.D. Wu, B. Gault, P. Kontis, D. Raabe, L. Gu, Q.H. Zhang, H.W. Chen, H.T. Wang, J.B. Liu, K. An, Q.S. Zeng, T.G. Nieh, Z.P. Lu, Nature 563 (2018) 546–550.
[15] X.R. Liu, S.D. Zhang, H. Feng, J. Wang, P. Jiang, H.B. Li, F.P. Yuan, X.L. Wu, Acta Mater. 255 (2023) 119079.
[16] S.W. Li, F. Liu, T.X. Si, C.C. Xue, W.R. Sun, Mater. Charact. 200 (2023) 112895.
[17] Y.S. Wu, X.Z. Qin, C.S. Wang, L.Z. Zhou, Mater. Sci. Eng. A 768 (2019) 138454.
[18] J.S. Rege, M.J. Hua, C.I. Garcia, A.J. Deardo, ISIJ Int. 40 (2000) 191–199.
[19] Y.Q. Weng, in: Ultra-Fine Grained Steels, 1st ed., Metallurgical Industry Press, Beijing, 2008, pp. 431–470.
[20] F.B. Pickering, Int. Mater. Rev. 211 (1976) 227–249.
[21] E. Jimenez-Melero, N.H. Van Dijk, L. Zhao, J. Sietsma, S.E. Offerman, J.P. Wright, S. Van Der Zwaag, Acta Mater. 57 (2009) 533–543.
[22] S.L. Yang, W.R. Sun, J.X. Wang, Z.M. Ge, S.R. Guo, Z.Q. Hu, J. Mater. Sci. Technol. 27 (2011) 539–545.
[23] D.B. Miracle, O.N. Senkov, Acta Mater. 122 (2017) 448–511.
[24] E.P. George, D. Raabe, R.O. Ritchie, Nat. Rev. Mater. 4 (2019) 515–534.
[25] B. Cantor, Prog. Mater. Sci. 120 (2021) 100754.
[26] B. Gludovatz, A. Hohenwarter, D. Catoor, E.H. Chang, E.P. George, R.O. Ritchie, Science 345 (2014) 1153–1158.
[27] B. Gludovatz, A. Hohenwarter, K.V.S. Thurston, H.B. Bei, Z.G. Wu, E.P. George, R.O. Ritchie, Nat. Commun. 7 (2016) 10602.
[28] M.X. Yang, D.S. Yan, F.P. Yuan, P. Jiang, E. Ma, X.L. Wu, Proc. Natl. Acad. Sci. U.S.A. 115 (2018) 7224–7229.
[29] D. Liu, Q. Yu, S. Kabra, M. Jiang, P. Forna-Kreutzer, R.P. Zhang, M. Payne, F. Walsh, B. Gludovatz, M. Asta, A.M. Minor, E.P. George, R.O. Ritchie, Science 378 (2022) 978–983.
[30] I. Moravcik, V. Hornik, P. Minárik, L.L. Li, I. Dlouhy, M. Janovska, D. Raabe, Z.M. Li, Mater. Sci. Eng. A 781 (2020) 139242.
[31] M.X. Yang, Y. Pan, F.P. Yuan, Y.T. Zhu, X.L. Wu, Mater. Res. Lett. 4 (2016) 145–151.
[32] X.L. Wu, M.X. Yang, F.P. Yuan, G.L. Wu, Y.J. Wei, X.X. Huang, Y.T. Zhu, Proc. Natl. Acad. Sci. U.S.A. 112 (2015) 14501–14505.
[33] S. Qin, M.X. Yang, P. Jiang, J. Wang, X.L. Wu, H. Zhou, F.P. Yuan, J. Mater. Sci. Technol. 153 (2023) 166–180.
[34] D.X. Wei, L.Q. Wang, Y.J. Zhang, W. Gong, T. Tsuru, I. Lobzenko, J. Jiang, S. Harjo, T. Kawasaki, J.W. Bae, W.J. Lu, Z. Lu, Y. Hayasaka, T. Kiguchi, N.L. Okamoto, T. Ichitsubo, H.S. Kim, T. Furuhara, E. Ma, H. Kato, Acta Mater. 225 (2022) 117571.
[35] J. Ding, Q. Yu, M. Asta, R.O. Ritchie, Proc. Natl. Acad. Sci. U.S.A. 115 (2018) 8919–8924.
[36] T. Yang, Y.L. Zhao, W.P. Li, C.Y. Yu, J.H. Luan, D.Y. Lin, L. Fan, Z.B. Jiao, W.H. Liu, X.J. Liu, J.J. Kai, J.C. Huang, C.T. Liu, Science 369 (2020) 427–432.
[37] J.S. Cao, F.C. Li, Q.H. Zhang, M.X. Li, C. Wang, W.H. Wang, Y.H. Liu, Scr. Mater. 234 (2023) 115545.
[38] Q.Q. Ding, Y. Zhang, X. Chen, X.Q. Fu, D.K. Chen, S.J. Chen, L. Gu, F. Wei, H.B. Bei, Y.F. Gao, M.R. Wen, J.X. Li, Z. Zhang, T. Zhu, R.O. Ritchie, Q. Yu, Nature 574 (2019) 223–227.
[39] G. Laplanche, A. Kostka, C. Reinhart, J. Hunfeld, G. Eggeler, E.P. George, Acta Mater. 128 (2017) 292–303.
[40] Y. Yuan, Y.F. Gu, C. Cui, T. Osada, Z.H. Zhong, T. Tetsui, T. Yokokawa, H. Harada, J. Mater. Res. 26 (2011) 2833–2837.
[41] Z. Wu, H. Bei, G.M. Pharr, E.P. George, Acta Mater. 81 (2014) 428–441.
[42] X.L. Wu, P. Jiang, L. Chen, F.P. Yuan, Y.T. Zhu, Proc. Natl. Acad. Sci. U.S.A. 111 (2014) 7197–7201.
[43] B.B. He, B. Hu, H.W. Yen, G.J. Cheng, Z.K. Wang, H.W. Luo, M.X. Huang, Science 357 (2017) 1029–1032.
[44] Q.S. Pan, L.X. Zhang, R. Feng, Q. Lu, K. An, A.C. Chuang, J.D. Poplawsky, P.K. Liaw, L. Lu, Science 374 (2021) 984–989.
[45] J. Rackwitz, Q. Yu, Y. Yang, G. Laplanche, E.P. George, A.M. Minor, R.O. Ritchie, Acta Mater. 200 (2020) 351–365.
[46] S. Yuan, B. Gan, L. Qian, B. Wu, H. Fu, H.H. Wu, C.F. Cheung, X.S. Yang, Scr. Mater. 203 (2021) 114117.
[47] D.E. Jodi, N. Choi, J. Park, N. Park, Metall. Mater. Trans. A 51 (2020) 3228–3237.
[48] Y.Y. Shang, Y. Wu, J.Y. He, X.Y. Zhu, S.F. Liu, H.L. Huang, K. An, Y. Chen, S.H. Jiang, H. Wang, X.J. Liu, Z.P. Lu, Intermetallics 106 (2019) 77–87.
[49] Z. Li, X. Long, S.Y. Zhang, H.W. Deng, M. Zhang, T. Zhang, Scr. Mater. 235 (2023) 115633.
[50] Y. Ma, F.P. Yuan, M.X. Yang, P. Jiang, E. Ma, X.L. Wu, Acta Mater. 148 (2018) 407–418.
[51] G. Laplanche, A. Kostka, O.M. Horst, G. Eggeler, E.P. George, Acta Mater. 118 (2016) 152–163.
[52] H. Van Swygenhoven, P.M. Derlet, A.G. Frøseth, Nat. Mater. 3 (2004) 399–403.
[53] Y.L. Zhao, T. Yang, Y. Tong, J. Wang, J.H. Luan, Z.B. Jiao, D. Chen, Y. Yang, A. Hu, C.T. Liu, J.J. Kai, Acta Mater. 138 (2017) 72–82.
[54] X.L. Ma, C.X. Huang, J. Moering, M. Ruppert, H.W. Höppel, M. Göken, J. Narayan, Y.T. Zhu, Acta Mater. 116 (2016) 43–52.
[55] X.X. Ding, J. Wang, D. Liu, C. Wang, P. Jiang, H. Qu, G.H. Liu, F.P. Yuan, X.L. Wu, Rare Met. 41 (2022) 2894–2905.
[56] S.D. Zhang, M.X. Yang, X.L. Wu, F.P. Yuan, Mater. Des. 225 (2023) 111473.
[57] Q.S. Pan, M.X. Yang, R. Feng, A.C. Chuang, K. An, P.K. Liaw, X.L. Wu, N.R. Tao, L. Lu, Science 382 (2023) 185–190.
[58] Y.S. Li, W.B. Liao, H.C. Chen, J. Brechtl, W.L. Song, W. Yin, Z.B. He, P.K. Liaw, Y. Zhang, Sci. China Mater. 66 (2023) 780–792.
[59] X.F. Chen, Q. Wang, Z. Cheng, M.L. Zhu, H. Zhou, P. Jiang, L.L. Zhou, Q.Q. Xue, F.P. Yuan, J. Zhu, X.L. Wu, E. Ma, Nature 592 (2021) 712–716.
[60] L. Wang, J. Ding, S.S. Chen, K. Jin, Q.H. Lu, J.X. Cui, B.P. Wang, B. Chen, T.Y. Li, Y. Ren, S.J. Zheng, K.S. Ming, W.J. Lu, J.H. Hou, G. Sha, J. Liang, L. Wang, Y.F. Xue, E. Ma, Nat. Mater. 22 (2023) 950–957.
[61] Y.F. Wang, X.L. Ma, F.J. Guo, Z.F. Zhao, C.X. Huang, Y.T. Zhu, Y.G. Wei, Mater. Des. 225 (2023) 111593.
[62] H. Chang, T.W. Zhang, S.G. Ma, D. Zhao, R.L. Xiong, T. Wang, Z.Q. Li, Z.H. Wang, Mater. Des. 197 (2021) 109202.
[63] L. Ding, A. Hilhorst, H. Idrissi, P.J. Jacques, Acta Mater. 234 (2022) 118049.
[64] J.K. Kim, B.C. De Cooman, Mater. Sci. Eng. A 676 (2016) 216–231.
[65] S. Curtze, V.T. Kuokkala, Acta Mater. 58 (2010) 5129–5141.
[66] M.J. Szczerba, M.S. Szczerba, Acta Mater. 133 (2017) 109–119.